A multiscale and multiphysics model of strain development in a 1.5 T MRI magnet designed with 36 filament composite MgB$_2$ superconducting wire

Abdullah Al Amin[1]**, Tanvir Baig**[2]**, Robert J Deissler**[2]**, Zhen Yao**[2]**, Michael Tomsic**[3]**, David Doll**[3]**, Ozan Akkus**[1] **and Michael Martens**[2]

[1] Department of Mechanical and Aerospace Engineering, Case Western Reserve University, Cleveland OH, USA
[2] Department of Physics, Case Western Reserve University, Cleveland OH, USA
[3] HyperTech Research, Incorporated, Columbus OH, USA

E-mail: ozan.akkus@case.edu and michael.martens@case.edu

Abstract

High temperature superconductors such as MgB$_2$ focus on conduction cooling of electromagnets that eliminates the use of liquid helium. With the recent advances in the strain sustainability of MgB$_2$, a full body 1.5 T conduction cooled magnetic resonance imaging (MRI) magnet shows promise. In this article, a 36 filament MgB$_2$ superconducting wire is considered for a 1.5 T full-body MRI system and is analyzed in terms of strain development. In order to facilitate analysis, this composite wire is homogenized and the orthotropic wire material properties are employed to solve for strain development using a 2D-axisymmetric finite element analysis (FEA) model of the entire set of MRI magnet. The entire multiscale multiphysics analysis is considered from the wire to the magnet bundles addressing winding, cooling and electromagnetic excitation. The FEA solution is verified with proven analytical equations and acceptable agreement is reported. The results show a maximum mechanical strain development of 0.06% that is within the failure criteria of -0.6% to 0.4% (-0.3% to 0.2% for design) for the 36 filament MgB$_2$ wire. Therefore, the study indicates the safe operation of the conduction cooled MgB$_2$ based MRI magnet as far as strain development is concerned.

Keywords: superconducting magnet, finite element analysis, superconductor mechanical property, mechanical stress and strain, magnesium diboride, conduction cooled, MRI

(Some figures may appear in colour only in the online journal)

1. Introduction

Magnetic resonance imaging (MRI) has evolved into an indispensable medical technology over the past three decades. The core of an MRI machine, the background magnet is designed and built with superconducting wire due to the demand for high magnetic field strengths of 1.5 T or more. With approximately 35 000 machines installed [1, 2] world-wide, the MRI industry is the leading market for superconducting wire. Currently, MRI magnet wires are mostly made of niobium titanium (NbTi) superconducting wire which has a critical temperature of 9 K [3]. As a result, the superconducting magnet needs to be operated well below 9 K for persistent mode operation. Typically, NbTi based MRI magnets are cooled down to 4.2 K using a liquid helium (LHe) bath. Most commonly used clinical MRI systems operate at a magnetic field strength of 1.5–3.0 T in the diametrical spherical volume (DSV). This magnet requires approximately 1500–2000 l of LHe to cool down initially and make it operational, in the plant while testing, and in the field

if the magnet quenches [4]. The price of helium has increased substantially in the last few years and is expected to continue to rise over the next several years because of a shortage of supply. With the burgeoning market of the MRI industry expected to reach $7.4 billion [4], the rising cost of LHe will contribute to the overall price and on-going maintenance of an MRI system. This expanding market for MRI coupled with decreasing helium reserves [5], has motivated the MRI scientific community to look for a favorable alternative to LHe in the design and operation of the main background magnet.

One of the alternatives to a LHe filled 'wet' magnet is to design a 'dry' magnet that can be conduction cooled using two stages of refrigeration. Such an MRI system would require very little LHe, on the order of 1–3 l, to set up the refrigeration system and cool down the cold head. The magnets [6, 7] are subsequently cooled via conduction to the cold head of the cryocooler. Higher temperature superconductors (HTS) such as MgB_2 ($T_c = 39$ K) [8], YBCO ($T_c = 93$ K) [7, 9], BSCCO ($T_c = 108$ K) [10] and Bi-2223 ($T_c = 90$–95 K) [11] are all good candidates for such conduction cooled magnet designs since their respective critical temperatures are much higher compared to NbTi. The underlying advantage of using HTS is the increased temperature margin for cryogenics designs that facilitate operation at relatively higher temperature gradients in the winding package and thus favoring the conduction cooled system. However, the conduction cooled system for a full body MRI magnet is still in progress and several undergoing works have demonstrated the feasibility of such superconducting wires for MRI magnet designs [6, 9, 11–13]. Among these available options, MgB_2 superconducting wire is of special interest due to its comparatively high mechanical stability, small mechanical and thermal anisotropy and high critical temperature of 39 K [14]. Since its discovery in 2001, several works have been published to show the viability of MgB_2 for MRI magnet designs that could operate at 10 K or more [8, 15–18]. Studies of MgB_2 wires to date have been experimental in context, assessing different types of monofilament [19] and multifilament [20, 21] wire configurations and showing promise as laboratory experiments exhibit increased ultimate failure strain, and critical current [22–28] carrying capability.

While there is an increasing focus on MgB_2 wires, the low failure strain of the MgB_2 wires [22, 23, 29, 30] increase the demand for knowledge of the strain distribution during coil design. A magnet experiences strain development caused by the applied pretension at the time of the winding process and anisotropic deformation caused by thermal contraction attributed to mismatched thermal strain of wire constituents and mandrel material. At the time of operation, the magnet is electrically charged and the Lorentz force generates more strain in the wire, this phenomenon has been numerically solved and experimentally verified [31]. It is critical to understand the strain development in magnetic coils of MgB_2 because of the low failure strain of the material. While multiscale and multiphysics FE analysis of NbTi superconducting magnets has been carried out by researchers [32–38], mechanical strain analysis of a conduction cooled MgB_2 based superconducting solenoid magnet is yet to be explored.

The purpose of this study is to develop a multiscale and multiphysics model to predict the final stress state in 1.5 T react-and-wind MgB_2 MRI coils following the production, cooling and magnetization stages. The model is multiphysics to account for mechanically, thermally and magnetically induced strains and it is multiscale because it executes a homogenization scheme to connect the wire scale to the coil scale.

We sought to model the strain distribution in MgB_2 coils by using finite element analysis (FEA) because the analytical solutions for studying strain in coils may be limited in terms of handling complex geometric shapes, imposed boundary conditions and in addressing the variation of elastic moduli between mandrel, epoxy and wire. Moreover, analytical solutions are generally limited to isotropic material properties whereas an orthotropic material property approximation for composite wire would be more realistic. As a result, current magnet designers rely mostly on computer programs based on FEA compared to analytical approaches such as filament winding of pressure vessels, [38, 39] thermal cooling [39] and electromagnetic charging [40]. Therefore, in this study we have calculated the total (accumulated) mechanical strain (ε_T) resulting from winding (ε_w), cool-down (ε_{th}), and electromagnetic charging (ε_e) experienced by the MgB_2 coil system.

2. Materials and methods

The manufacturing and operation of an MRI magnet system undergoes three different stages—the winding of superconducting wire around a mandrel, the thermal cool-down of the entire system to the operating temperature of 10 K and the charging of the system electromagnetically by passing the design current through the wire.

In this article, a 1.5 T MgB_2 based 36 filament superconducting wire is used to manufacture each coil bundle by winding the wires around a non-ferromagnetic stainless steel mandrel. During the winding process, typically a 7–15 lb pretension is applied on the wire to ensure adequate packing. In order to analyze the MRI system for maximum strain development, 31.14 MPa (15 lb) of pretension is considered to be applied on the wire at the time of the winding process. This process is similar for all the five bundles considered in the 2D axisymmetric computational model. After the winding process, the magnet bundles are assembled into the vacuum vessel and the copper straps connected to the bundle for conduction cooling are linked to the second stage of the cryocooler. The entire assembly is thermally shielded inside an aluminum thermal shield. Next, the evacuated space containing the mechanically integrated coils and insulation are subjected via cryocoolers to a uniform thermal gradient in order to model the cool-down of the entire system from room temperature of 298 K to the operating temperature at the coils of 10 K. Once, the system is cooled down to the operating temperature, the magnets are then energized with an operating current of 255.87 A, which corresponds to an engineering current density of 118.5 A mm^{-2} to generate a magnetic field of 1.5 T in the DSV. The process affecting the MgB_2 wire
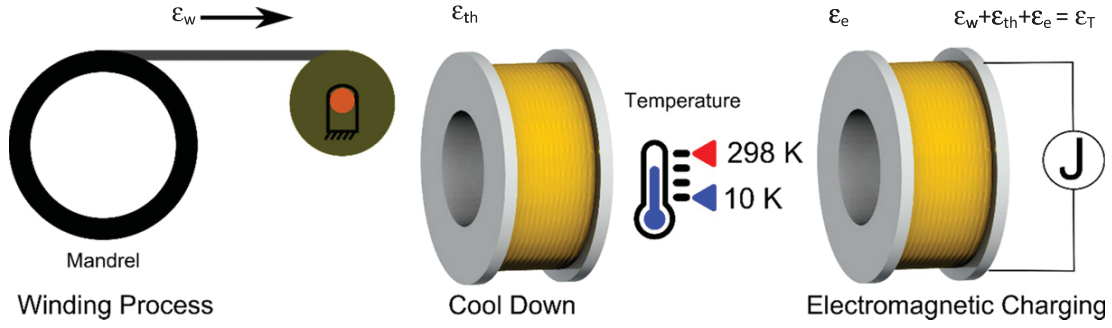
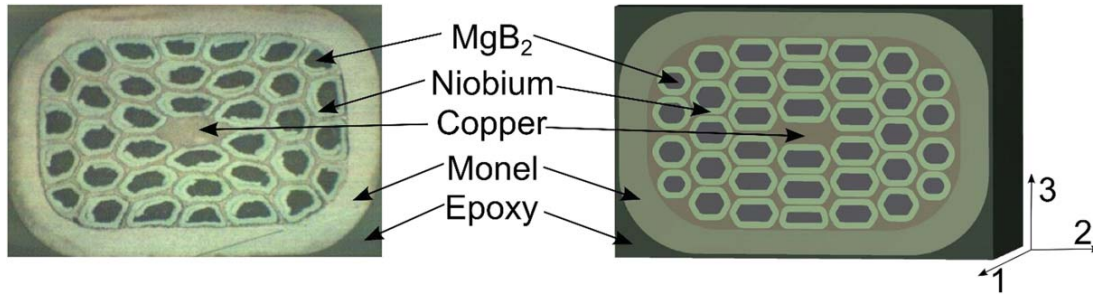**Figure 1.** Manufacturing process of a superconducting solenoid.

Figure 2. Wire cross section of 36 filament MgB_2 based superconducting wire. Microscopic picture on left and computer aided designed (CAD) model on right. The orthogonal directions 1, 2, and 3 are shown in the figure.

performance starting with winding and ending with electromagnetic charging is summarized in figure 1. As mentioned before, a 36 filament MgB_2 based superconducting wire is considered for the MRI system. As the modeling of an entire bundle considering each wire constituent individually would be computationally intensive, the wire is first analyzed and numerically homogenized as an orthotropic material. This wire length scale considers the wire constituents, MgB_2, niobium, copper, monel and epoxy as isotropic. The homogenized wire material properties then substitutes for the material properties of the coil bundle considering complete orthotropy, which is the coil bundle length scale. The coil bundles are solved for all three processes—winding, cooldown and electromagnetic excitation. There are well verified existing analytical approaches [33, 34, 36–38] to model winding, thermal cool down [39] and electromagnetic charging [31, 40–44], but the computational approach based on FEA is well favored considering orthotropic material approximation, boundary conditions, geometric complexity, and multivariate elastic moduli of wire and mandrel. Hence, while employing FEA analysis; shifting from the wire length scale to the coil bundle length scale makes the problem multiscale and modeling the coil bundle for electromagnetic excitation stress–strain turns the model into multiphysics modeling. Hence, a multiscale multiphysics model is required for the entire 1.5 T MRI magnet bundle.

3. Wire configuration and material properties

The wire considered for the design has dimensions of 1.19 mm by 1.82 mm including insulation (figure 2). The composite wire has a total of 36 filaments of MgB_2 (volume fraction 18%) enclaved by a layer of Niobium (25%) inside a Copper (16%) matrix. The entire matrix is surrounded by Monel (29%). The entire wire is enveloped by a layer of epoxy of commercial grade (12%).

Since the modeling of the individual wire explicitly in a bundle would be cumbersome and computationally intensive a numerical homogenization approach as detailed by Barbero [45] and introduced by Luciano [46] is employed to approximate material properties of the composite wire as orthotropically elastic. A similar approach to modeling material properties of Nb_3Sn wire strands has also been implemented by Collins [47] and Boso [48, 49]. A full wire model of the representative volume element (RVE) is designed and meshed to which unit normal and shear strains are applied one at a time [46]. This applied unit strain results in a complex state of strain inside the RVE, which is averaged over the RVE and components of the elastic matrix are approximated from the averaged strain state. The constituent and calculated material properties are summarized in tables 1 and 2. The homogenized material property values are used in the analysis of all five bundles in the 1.5 T system.

Table 1. Material property of wire constituents and Mandrel.

Material	Modulus of elasticity (GPa) at 298 K	Poisson's ratio (ν) at 298 K	Average thermal expansion coefficient (10–298 K) μm m^{-1} K^{-1}
MgB$_2$	273 [50]	0.181 [50]	4.23 [51]
Copper	129.5 [52]	0.355	10.9 [52]
Niobium	103 [53]	0.4 [53]	9.28 [54]
Monel	179 [55]	0.315 [55]	12.5 [55]
Epoxy	19.7 [56]	0.355	19.83(through thickness), 6.23 (warp or fill) [56]
302 stainless steel	190 [57]	0.305	12

Table 2. Summary of material properties of wire.

Material property (directions are shown in figure 2)	Homogenized 36 filament wire
Modulus of elasticity (direction 1)	153 GPa
Modulus of elasticity (direction 2)	123 GPa
Modulus of elasticity (direction 3)	119 GPa
Shear modulus (direction 1–2)	43.9 GPa
Shear modulus (direction 2–3)	36.1 GPa
Shear modulus (direction 3–1)	40.9 GPa
Poisson's ratio (direction 1–2)	0.284
Poisson's ratio (direction 2–3)	0.332
Poisson's ratio (direction 3–1)	0.291
Average thermal expansion coefficient (10–298 K) (α_{23})	10.79 μm m^{-1} K^{-1}
Average thermal expansion coefficient (α_1)	9.26 μm m^{-1} K^{-1}

4. Coil and mandrel geometry

The coil design under consideration is a 1.5 T magnetically shielded, full-body system consisting of ten coils and an engineering current density of 118.5 A mm^{-2} (figure 3). Since this system is symmetric about the mid-plane, the total geometry reduces to quarter symmetry, which saves computational effort. The dimensions of the coil windings for the entire magnet system are provided in table 3.

4.1. Winding stress

The amount of pretension on the wire depends on the magnetic field design, wire cross section and strain limitation of wire materials. For a 1.5 T MRI system, a maximum 31.14 MPa pretension is fairly common for this wire size and will be assumed for modeling of the bundle winding.

4.1.1. Winding stress prediction by analytical approach.
Before the availability of high performance computational resources, the stress–strain equations were solved analytically to estimate the effect of winding stress. One approach to address the prestressing of the wire is to change the effective elastic modulus of the material as the wire is prestressed during winding around the mandrel [39]. Several other methods were also investigated in which each layer of a coil bundle is approximated as concentric thin cylinders [33, 38]. However, all of the analytical approaches are based on a

stress–strain relation, which takes the form of Hooke's law when simplified. The equation in contracted notation becomes,

$$\varepsilon_i = \frac{\sigma_i}{E_i} - \sum_{\substack{j=1 \\ j \neq i}}^{3} \nu_{ji} \frac{\sigma_j}{E_j}, \quad i = 1, \ 2, \ 3, \tag{1}$$

where σ_i, ε_i and E_i are the stress, strain and elastic modulus in three orthogonal direction (r, θ and z), respectively, and ν_{ij} is Poisson's ratio. Since the stress in the axial direction of the bundle (direction 2 of wire) is negligible compared to the applied winding tension, the plane-stress approximation is more appropriate than the plane-strain [39]. When a layer of the bundle is wound with pretension, the applied radial pressure on the lower layers can be calculated by considering each layer of a coil as a concentric homogeneous cylinder using the following equation [33, 38].

$$p_k = \frac{\sigma_{w_0,k} t_k}{r_1 + \sum_{j=1}^{i} t_j} = \frac{\sigma_{w_0,k} t_k}{r_{w,k}}. \tag{2}$$

Here, $\sigma_{w_0,k}$ is the winding prestress on the kth layer, t_k is the thickness of the kth layer, r_1 is the inner radial distance of the first layer of the coil, and t_j is the thickness of each of the wound layers. The hoop stress developed on the lower layers due to this applied pressure becomes

$$\sigma_{\theta i} = \frac{p_k \left(r_1 + \sum_{j=1}^{i-1} t_j \right)}{\sum_{j=0}^{i-1} t_j}. \tag{3}$$

If the layer itself is wound with a prestress, σ_k, this amount of pretension will superpose with the calculated circumferential stress given by equation (3). Hence, the total hoop stress developed due to winding of the kth layer (σ_{wk}) would be

$$\sigma_{wk} = \sigma_{w_0,k} + \sum_{i=k+1}^{n} \sigma_{\theta i}. \tag{4}$$

The calculation of circumferential stress using these equations are known as the combined homogeneous cylinder method (CHCM) [38]. In this paper, the CHCM analytical approximation is used to help validate the calculations of FEA. However, CHCM is limited by the inability to predict the stress development if there are multiple materials, each with a different elastic modulus.
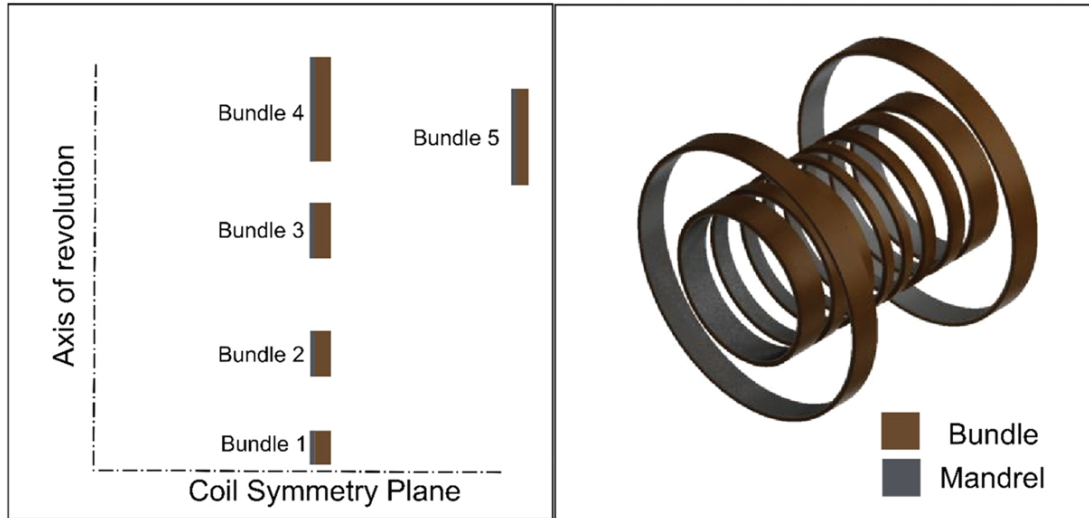
Figure 3. 2D axisymmetric (left) view of the coil half and isometric view (right) of the coil bundles assembly.

Table 3. Design specifications of 1.5 T conduction cooled MgB$_2$ superconducting magnet.

Coil	Inner radius (m)	Outer radius (m)	Starting axial position (m)	Ending axial location (m)
Bundle 1	0.5001	0.5321	0.0496	0.1167
Bundle 2	0.5005	0.5327	0.2273	0.3181
Bundle 3	0.5000	0.5321	0.4639	0.5764
Bundle 4	0.5000	0.5321	0.6595	0.8699
Bundle 5	0.9059	0.9309	0.6122	0.8063
Current density, $J = 118.5$ A mm^{-2}				

4.1.2. Winding stress prediction by FEA. ANSYS, a commercial FEA software, is used to model the winding process of a 1.5 T conduction cooled MgB$_2$ based superconducting magnet system. The basic equation for the FEA is summarized with the simplest equation as,

$$\{\sigma\} = [\mathrm{D}]\{\varepsilon^{\mathrm{el}}\}. \tag{5}$$

In the equation, [D] is the elastic stiffness matrix, $\{\varepsilon^{\mathrm{el}}\}$ represents the elastic strain vector, and $\{\sigma\}$ indicates the stress developed on the modeled geometry. To imitate the winding process, the element birth and death technique in ANSYS is employed. Quadratic 2D element Plane 183 is chosen for the geometry since the problem is considered 2D axisymmetric for simplification. Quadratic elements are chosen over linear elements (Plane 182) because they better approximate the stress at the mandrel-bundle interface with their shape functions. The initial state condition is used to apply the prestrain that corresponds to pretension of 31.14 MPa on the designated wire. After modeling the entire geometry, a uniform prestrain is applied to the coil bundle and all corresponding layer elements are deactivated by setting the stiffness to an ANSYS defined low value of 10^{-6}. Then, to imitate the winding process, each layer is activated by
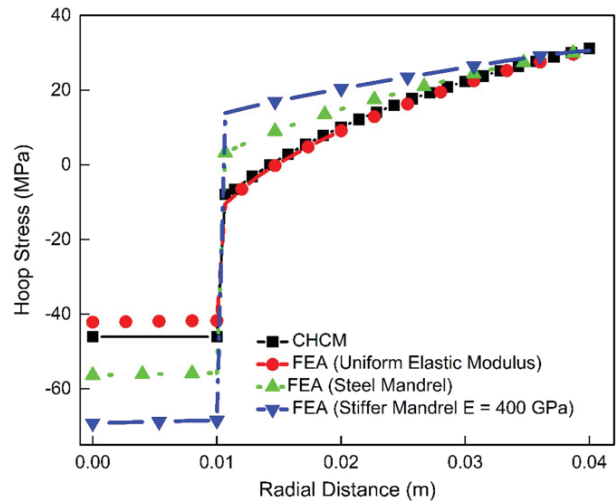

Figure 4. Comparison of finite element and analytical approach of solving the winding stress development in coil bundle 5 of the system.

returning the stiffness values to the actually assigned material property values. In order to compare the agreement between the analytical and FEA approaches, the outermost coil bundle (bundle 5 in figure 3) is modeled and compared for both the analytical and FEA results. It is clear from figure 4 that the analytical CHCM model is incapable of precisely calculating the stress as the value of the elastic modulus changes due to the change from stainless steel mandrel to coil bundle. This is because the CHCM equations do not consider the modulus of elasticity of different materials. On the other hand, the hoop stress values are within ~3% in the coil bundles if the mandrel and coil are made of the same material. Hence, the analytical CHCM method can be used to validate the FEA result, but cannot address the change in material stiffness values, which limits the use of CHCM in a mandrel-bundle winding modeling system.

4.2. Thermal cool-down stress

Once the construction and assembly of the magnet system is complete, the next step is to cool the magnet from room temperature to the cryogenic temperature of 10 K that is required for MgB_2 to act as a superconductor at optimum performance. This cooling down of the entire system creates stresses because, the thermal strain behavior of the mandrel and coil bundles is different and each is highly non-linear.

4.2.1. Thermal cool-down stress prediction by analytical approach.
As the temperature drops from room temperature (T_0) to a cryogenic temperature (T_f) the added effect on the strain in cylindrical coordinates due to the temperature change is expressed as,

$$\varepsilon_r = \frac{\partial u}{\partial r} - \int_{T_0}^{T_f(r)} \alpha_r dT, \quad \varepsilon_\theta = \frac{u}{r} - \int_{T_0}^{T_f(r)} \alpha_\theta dT. \quad (6)$$

The linear coefficient thermal expansion in the radial and circumferential directions is given as α_r and α_θ, respectively; these are functions of temperature. By implementing a simple power series expansion, Arp *et al* [39] presented the expression for hoop stress as

$$\sigma_\theta = \frac{kcr^{k-1}}{kL - V} + \frac{kdr^{-k-1}}{kL + V} + \sum_{i=0}^{n} \frac{1+i}{L} \frac{l_{ri} - (1+i)l_{\theta i}}{(1+i)^2 - k^2} r^i. \quad (7)$$

The terms L, V, k, c, and d are defined as:

$$L = \frac{1 - \nu_{\theta z}\nu_{z\theta}}{E_\theta},$$

$$V = \frac{\nu_{\theta r} + \nu_{\theta z}\nu_{zr}}{E_r},$$

$$k = \left(\frac{E_\theta}{E_r}\right)^{\frac{1}{2}},$$

$$c = \frac{kL - V}{L\left(\left(\frac{b}{a}\right)^k - \left(\frac{a}{b}\right)^k\right)}$$

$$\times \sum_{i=0}^{n} \frac{[l_{ri} - (1+i)l_{\theta i}]\left(\frac{a^{1+i}}{b^k} - \frac{b^{1+i}}{a^k}\right)}{(1+i)^2 - k^2},$$

$$d = \frac{kL + V}{L\left(\left(\frac{b}{a}\right)^k - \left(\frac{a}{b}\right)^k\right)}$$

$$\times \sum_{i=0}^{n} \frac{[l_{ri} - (1+i)l_{\theta i}](a^{1+i}b^k - b^{1+i}a^k)}{(1+i)^2 - k^2}, \quad (8)$$

where $\nu_{\theta z}$ and $\nu_{z\theta}$ are Poisson's ratio and E_θ and E_r are the modulus of elasticity of the material in the specified directions and 'a' and 'b' are the inner and outer radii of the cylinder.

4.2.2. Winding stress prediction by FEA.
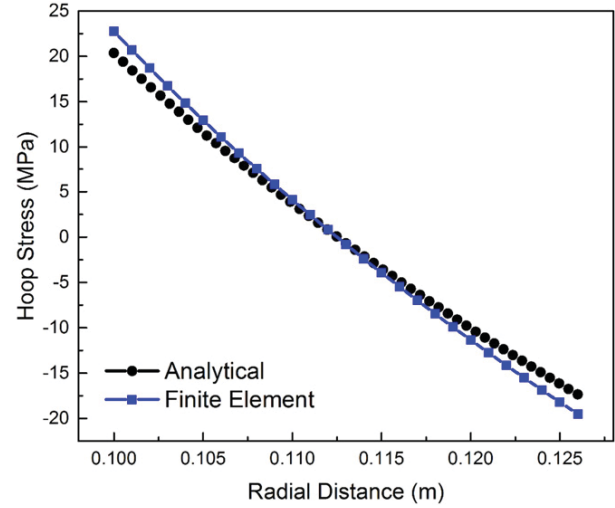In order to validate the FEA method with the analytical equations, the same

Figure 5. Comparison of finite element versus analytical solution of cool-down (298–10 K) of a solenoid considered by Arp.

superconducting solenoid considered by Arp [39] was solved and compared in figure 5. In ANSYS, quadratic plane element Plane 183 is used, and the linear thermal expansion coefficient is assigned in both the radial and circumferential (hoop) directions with the reference temperature set to T_0 (298 K). The temperature of the magnet is assumed to be spatially uniform during the entire cool down process from T_0 to T_f. The FEA equation now has the extra thermal strain term due to temperature change as shown in equation (9).

$$\{\sigma\} = [D](\{\varepsilon\} - \{\varepsilon^{th}\}). \quad (9)$$

The thermal strain $\{\varepsilon^{th}\}$ in the equation is calculated according to equation (6) as $\varepsilon^{th} = \int_{T_0}^{T_f(r)} \alpha dT$ and $\{\varepsilon\}$ is the total strain vector.

4.3. Electro-magnetic stress

When the superconducting solenoid is energized, the electromagnetic forces are determined from the radial and axial components of $\mathbf{J} \times \mathbf{B}$ where $\mathbf{J}$ and $\mathbf{B}$ are the vector representation of the current density and magnetic field, respectively. These radial and axial directional forces, when considered as a body force in the stress equation, result in stresses in the radial and hoop directions. The hoop stress appears to be dominating compared to the radial stress [41] and hence is of major concern when designing the superconducting solenoid.

4.3.1. Analytical approach.
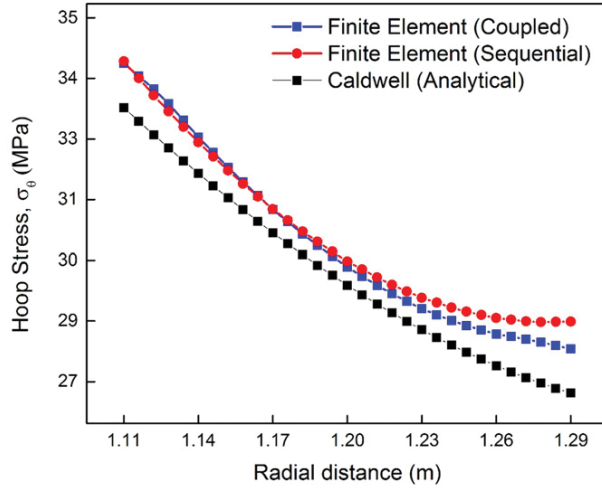At the time of electromagnetic charging, the stress–strain equations have another added term

Figure 6. Comparison of hoop stress variation along the radial direction of a solenoid. The analytical approach as provided by Caldwell [40] is in good agreement with the two different FEA approach using ANSYS.

from the Lorentz force. So the equation becomes:

$$r\frac{\partial \sigma_r}{\partial r} + (\sigma_r - \sigma_\theta) + X_r = 0, \qquad (10)$$

where X_r is the body force which relates to the magnetic field B_z as

$$X_r = JB_z \qquad (11)$$

and B_z is the axial component of the magnetic field. Caldwell [40], has derived the equation for hoop stress for a uniform solenoid in a final form as

$$\sigma_\theta = \frac{J\left\{B_1(r_2^2 + r_1r_2 - 2r_1^2) + B_2(2r_2^2 - r_1r_2 - r_1^2)\right\}}{6r\,\ln\left(\dfrac{r_2}{r_1}\right)}, \qquad (12)$$

where, B_1 and B_2 ar the radial component of the magnetic field at the inner radius (r_1) and outer radius (r_2)

4.3.2. Finite element analysis. ANSYS coupled field element Plane 13 (figure 6) is used to model the stress due to electromagnetic charging. ANSYS provides two different methods: sequential load transfer and direct coupled field analysis. For the former, Maxwell's equations are solved first and then forces at each nodal location are calculated. At the next step, the nodal forces are transferred to a new analysis, where the stress–strain equations are solved. In contrast, in the direct coupled analysis, the stress and strains are a direct output of the coupled electromagnetics and solid mechanics equation. The two different FEA analyses, direct coupled and sequential coupled field, are employed to model Caldwell's [40] superconducting solenoid and then compared with the analytical solution. However, ANSYS's limitation of handling load transfer from previous analyses (winding and cool-down) for a direct couple field analysis restricts the

solution method to sequential coupling. Figure 6 shows the agreement between the direct coupled, the sequential coupled and the analytical solution. It appears that the implementation of the sequentially coupled solution introduces a slight deviation from the direct coupled solution, but the variation is within 5% of the analytical range.

5. Results

The radial stress and strain for each bundle are plotted in figure 7 along the radial direction from the inner surface of the mandrel to the outer surface of the outermost layer of each coil bundle. Coil bundles 1 through 4 have the same number of winding layers with almost the same radial positions. Hence, the radial stress and strain developments in the coil bundle after winding are almost the same. From figure 7, it is noted that the maximum radial stress occurs within the coil near the boundary between the wires and the mandrel. The stresses are zero at the inner and outer boundary surfaces as these two boundaries are free to move in the radial direction. This application of winding stress helps compensate for the tensile stress developed from the magnetic forces during operation [39], and thus assists in minimizing the developed strains, while keeping them within the failure limit. The pretension also helps to compensate for the transverse shear stress created by the Lorentz force [58] at the time of magnet operation and prevents the sliding of the layers relative to one another. This can be confirmed by comparing the strain development on the bundle at two stages: after winding and after electromagnetic charging. Moreover, pretension also helps in reducing the strain in the epoxy and reduces the possibility of the epoxy cracking [59]. Furthermore, Arp *et al* [39] showed that it is possible to control more precisely the total stress development at the time of electromagnet charging if the applied pretension is varied on the layers of the coil. These findings underscore the importance of controlling the pretension on the wire during the winding process of a superconducting solenoid.

When considering the stress and strain results from the structural analysis of a superconducting magnet bundle, it is found that the radial stresses are negligible compared to the hoop (circumferential) stresses. It is clear from figure 8 that the hoop stress varies in the range of −50 to 30 MPa, whereas the radial stress reaches only a maximum value of −1 MPa. Hence, previous works have looked into hoop stress (circumferential stress) [33, 35, 38] and von Mises stress [36, 37] to determine the failure criteria. However, in the numerical modeling, the wire inside the bundle is a composite wire made of certain proportions of MgB_2, niobium, copper, monel and epoxy. Hence, the superconducting filaments of MgB_2 act as a fiber–matrix composite, which undergoes tensile or compressive loading as the magnet is built, cooled down and charged. As summarized by Orifici *et al* [60] for composite fibers under tensile loading, it is usually the maximum strain that predicts the fiber failure. Besides, Vaghar *et al* [61] has included von Mises strains as one of the failure criteria for their Nb_3Sn superconducting magnets design. So it is
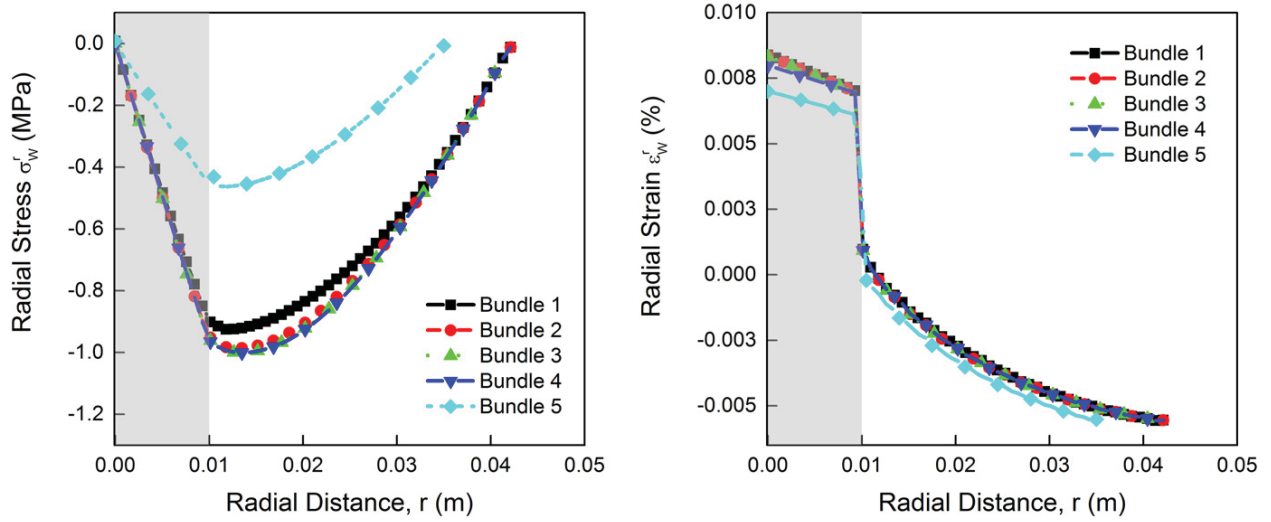
Figure 7. Radial stress along the radial direction of the mid-plane of all five coil bundles. (Mandrel regions are shaded in gray.)
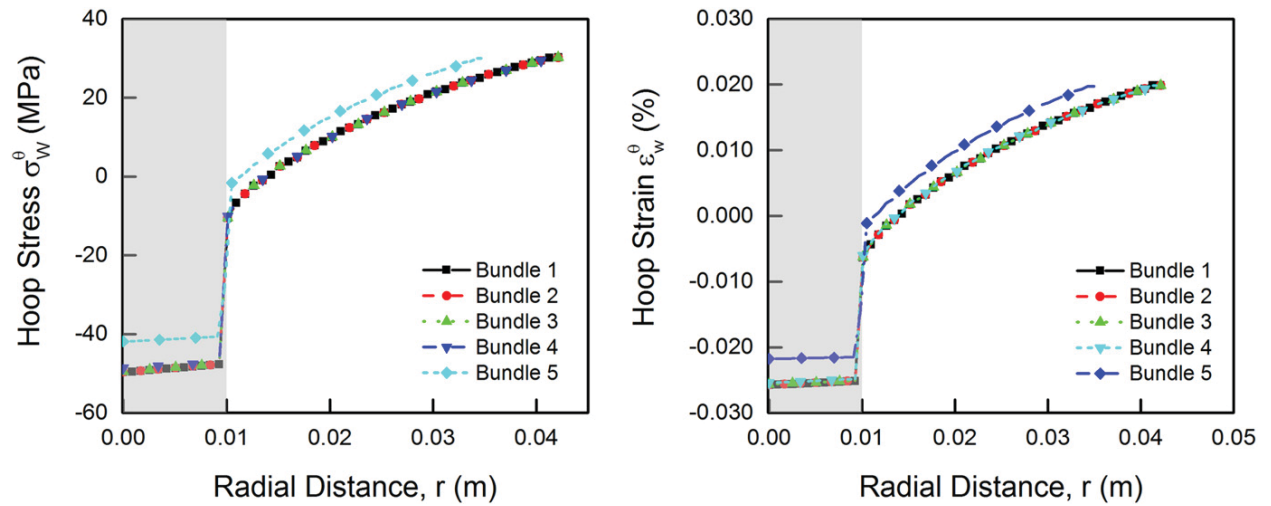

Figure 8. Hoop stress and strain plot along the radial direction of five bundles of the system.

important to consider the principal and von Mises stress and strains along with hoop (circumferential) stress and strains of the coil bundle. Moreover, uniaxial tensile testing of the superconducting wire at cryogenic temperatures reveals that the wire becomes resistive if the mechanical strain goes below -0.6% or above 0.4% [22, 23, 29, 62]. Therefore, it is also important to plot the third principal stress and strain as well in order to check if the magnet wire experiences mechanical strain below -0.6% at any point during the magnet operation. Hence, as a means of visualizing the stress and strain scenario, different types of stresses and strains are plotted for bundle 5 after the winding is complete (figure 9). From the figure, it is seen that both the tensile and compressive stress and strain scenarios are better picked up by the 1st and 3rd principal stresses and strains in the bundle coordinate system. This is due to the fact that $\sigma_1 > \sigma_2 > \sigma_3$ according to the definition of principal stress; where $\sigma_1, \sigma_2, \sigma_3$ are the stresses in the three principal directions respectively. Hence, if the

bundles are checked for tensile stresses and strains, σ_1 and ε_1 would provide the scenario where the bundle materials are in tensile loading. Correspondingly, for a compressive loading, the 3rd principal stress and strain would provide the bundle scenarios. On the other hand, the Von Mises stress and strain are limited in predicting the failure of a composite fiber–matrix configuration, because composite structures will individually have different compressive and tensile strengths, which do not meet the requirement of von Mises equivalent stresses and strains to be used as failure criteria [63]. Moreover, the von Mises stress and strain never go below zero and fail to predict the compressive stress and strains. As a result the first and third principal stresses and strains are considered as primary failure criteria for the design and thus plotted to give an overview of the stress–strain scenario of the magnet bundles. The stress–strain state after the winding is complete is summarized in figure 10. From this figure, it is noted that the first four bundles having the same inner and outer radii
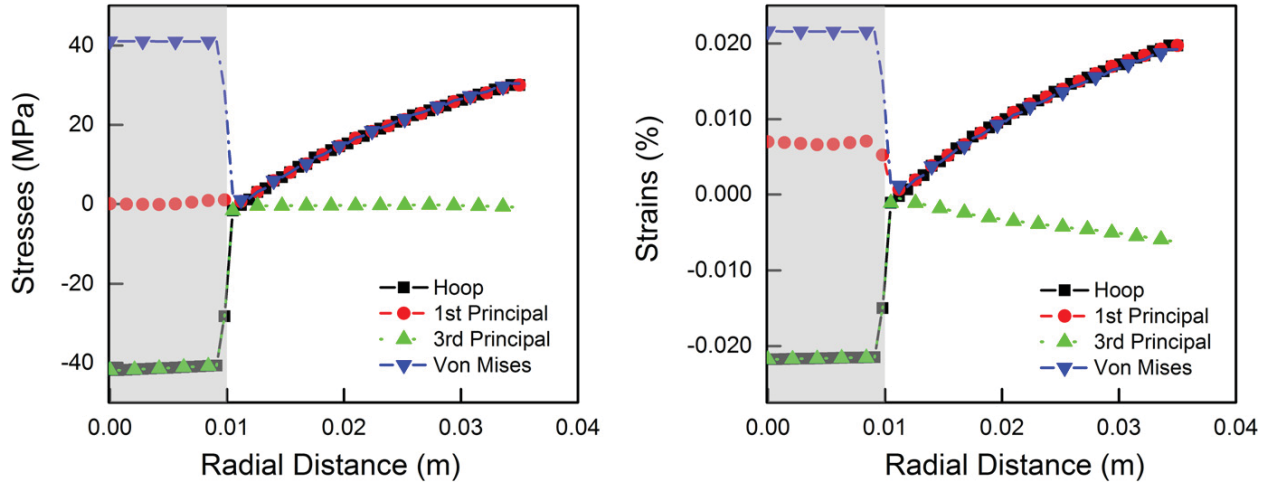
Figure 9. Four different types of stresses and strains on the coil bundle 5 along the radial direction after the winding of layers around the mandrel is complete.
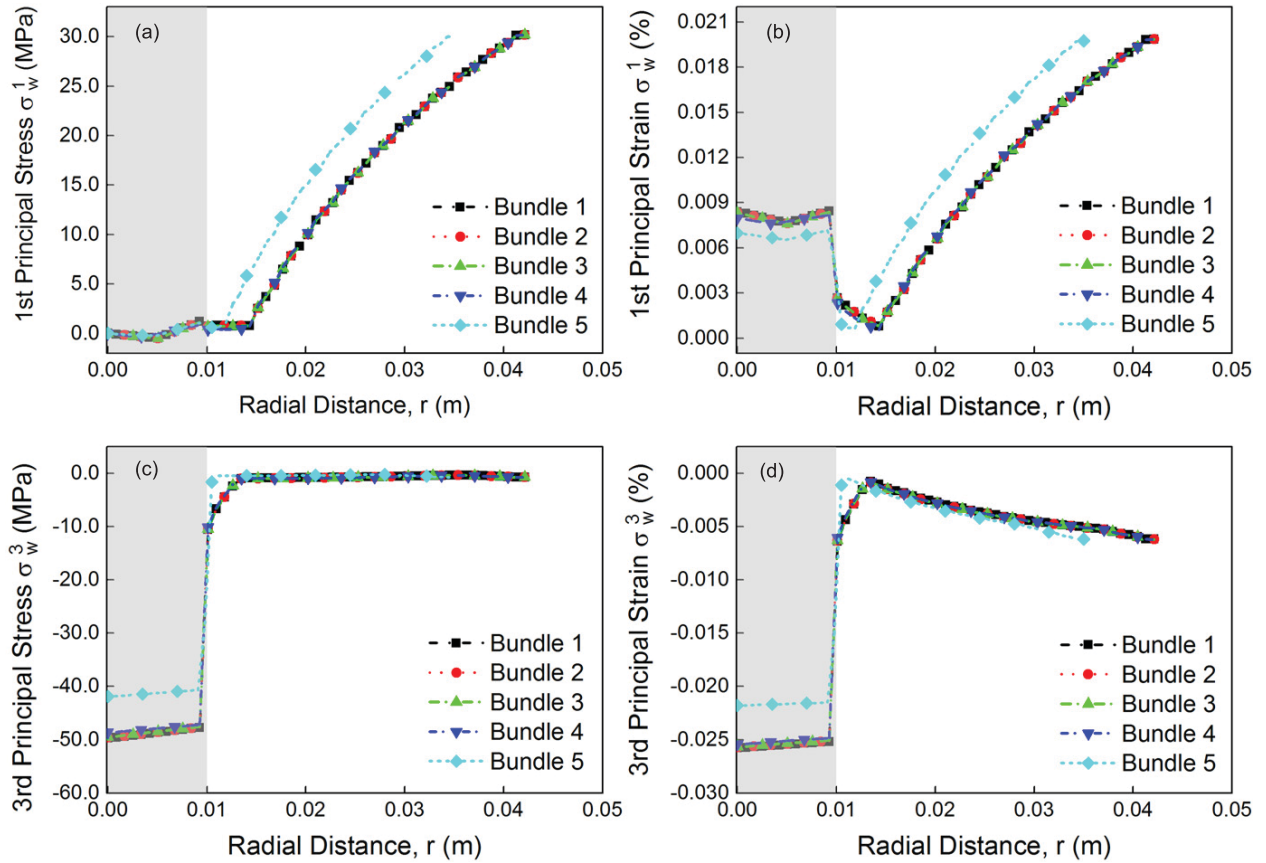

Figure 10. 1st and 3rd principal stress ((a), (c)) and strains ((b), (d)) along the radial distance of the all five coil bundles.

exhibit similar stress and strain development as to be expected and hence they are superposed. However, since the fifth bundle has a different radial thickness and different radial location, it has slightly different stress and strain development. The maximum tensile stress of 30 MPa is experienced by the bundles at the outermost layers. In contrast, the 3rd

principal stresses are peaked near the inner surface of the mandrel (-50 MPa). The peak values for 1st and 3rd principal strains are 0.019% and -0.025%, respectively.

The stress–strain scenario changes as the system is cooled down to an operating temperature of 10 K. Since, the mandrel is made of stainless steel, with a higher thermal
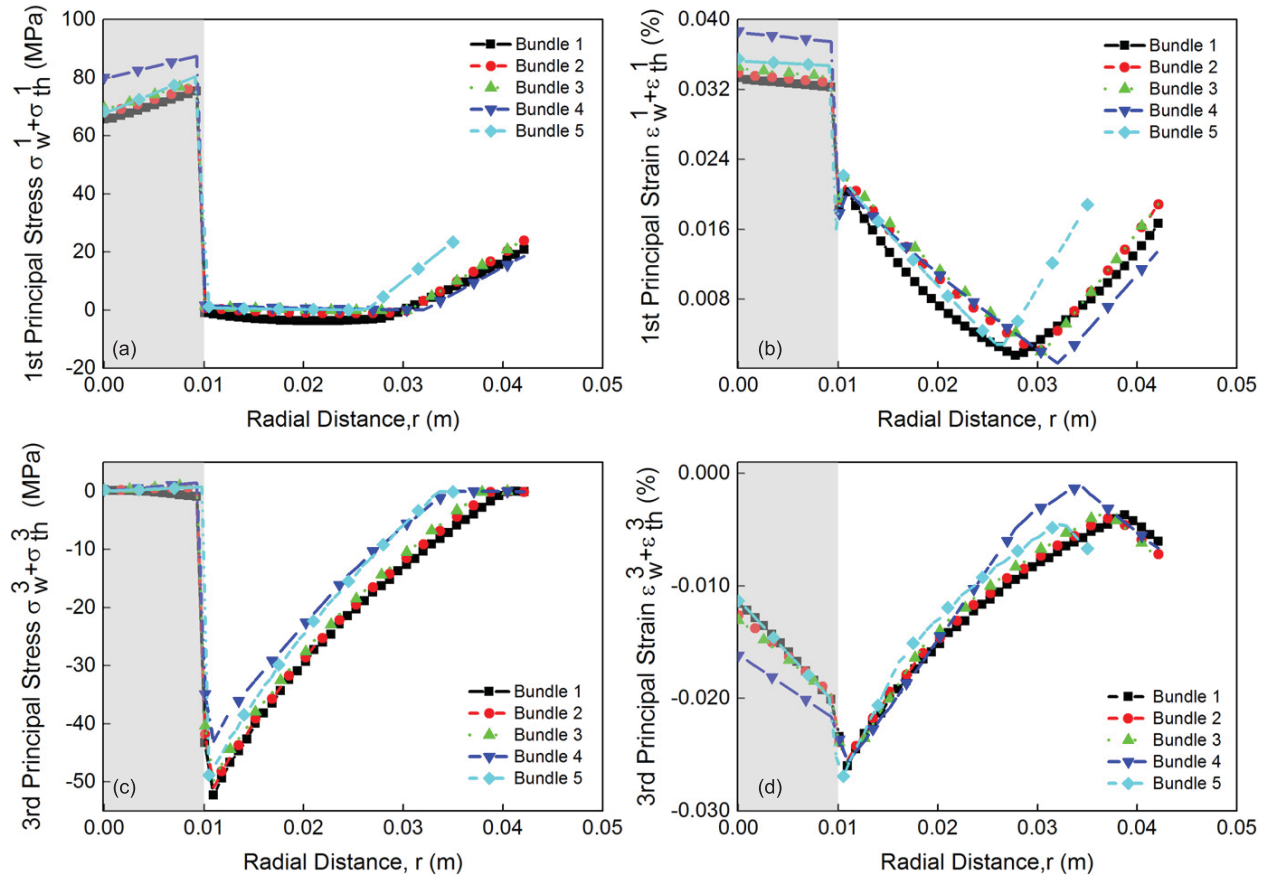
Figure 11. 1st and 3rd Principal mechanical stress ((a) and (c)) and strain ((b) and (d)) after the bundles are cooled down to operating temperature of 10 K.

expansion coefficient than the composite wire material, the mechanical strains determine the failure criteria [64]. Therefore, total mechanical strains ($\varepsilon_w + \varepsilon_{th}$) are to be checked for the failure criteria. Hence, total mechanical strains are plotted in figure 11 to visualize the strain development in the entire system. The thermal expansion coefficient of stainless steel is larger than for the wire; thus, the mandrel tends to shrink more relative to the wires as the temperature drops. As the temperature is dropping, the layers adjacent to the mandrel are pulled by the mandrel on one side, but restrained by the upper layers on the other side, which would generate a tensile loading along the radial direction. This occurrence of the tensile load is responsible for the sudden change in the 1st and 3rd principal strains in that region. The 1st and 3rd principal mechanical stress and strains are also plotted in figure 11. From the figure, the maximum tensile stress of ∼87 MPa is observed near the mandrel outer surface and maximum compressive stress of ∼52 MPa is observed to be developing near the innermost layers. The strains also peaks near ∼0.039% at the mandrel inner surface, whereas the compressive strain peaks at 0.026% near the first layer of the bundle. It is interesting to note that the strain curves for the first four bundle now have slight deviations from each other

caused by their different axial lengths due to the effect of added strain from thermal contraction.

At the time of operation, the Lorentz forces act on the coil bundle. This force is directed primarily radially outward on the bundles and generates tensile stress in the bundle layers. From the winding and thermal cool down process, there are residual compressive stresses already present in the mandrel and coil layers. The tensile stress generated counteracts the residual compressive stress and explains the importance of applying pretension in the wire at the time of the winding process. A careful design of applied pretension allows more room for electromagnetic stress development before the wire bundle crosses the design limit of strains as previously described. From the principal stress and strain plot (figure 12), it is observed that the maximum tensile stress develops in the mandrel outer radius, whereas the stress in the coil bundle peaks at ∼25 MPa. As far as the strain development is concerned, the maximum tensile strains of 0.016% occur in the innermost layer of the bundle. Some other researchers [22, 23, 29, 30, 62] have shown that the critical current carrying capacity of composite wire reduces as the strain is being developed. So the strain development in the wire bundle as a design criteria must stay below the limit of 0.2% (half of the failure criteria) in the tensile direction and
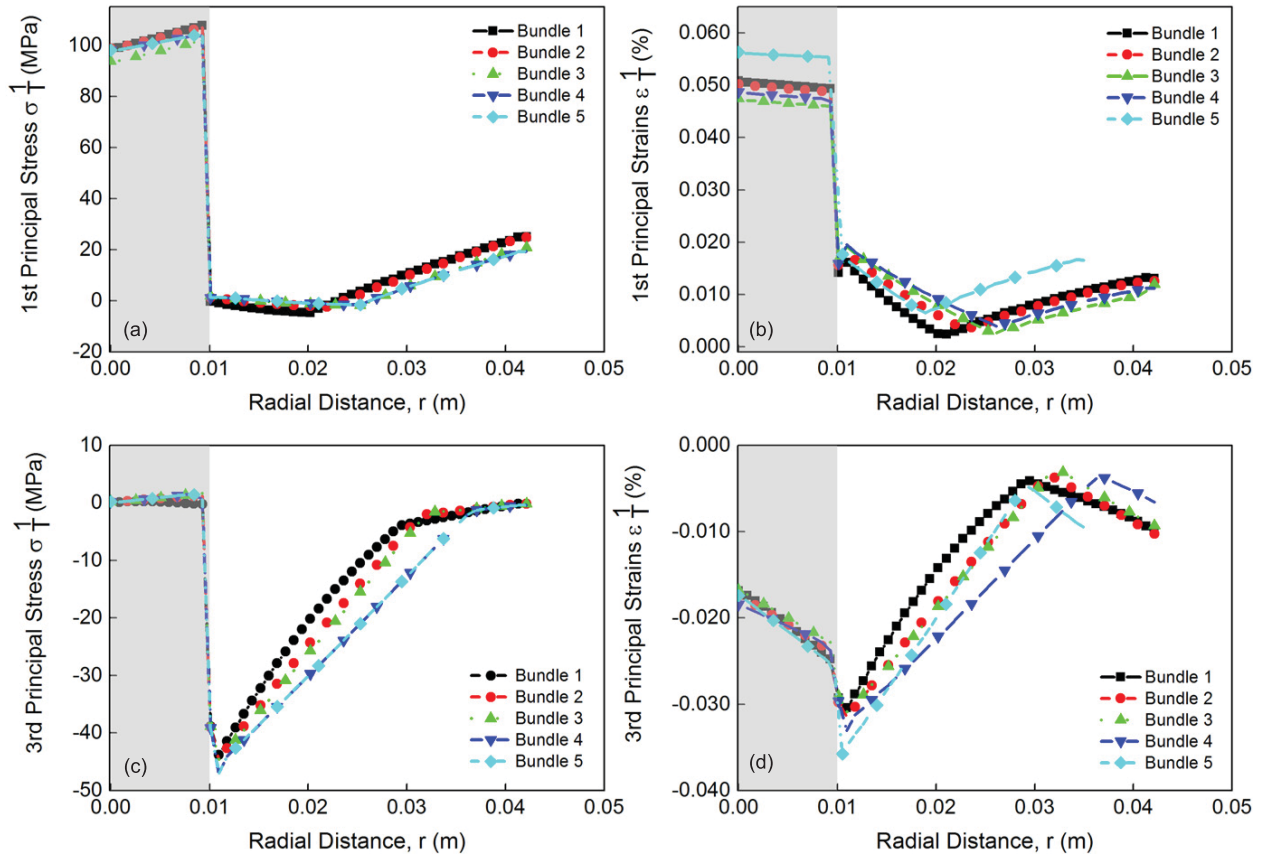
Figure 12. 1st and 3rd principal mechanical stresses ((a) and (c)) and strains ((b) and (d)) after the coil bundles are charged with the operating current.
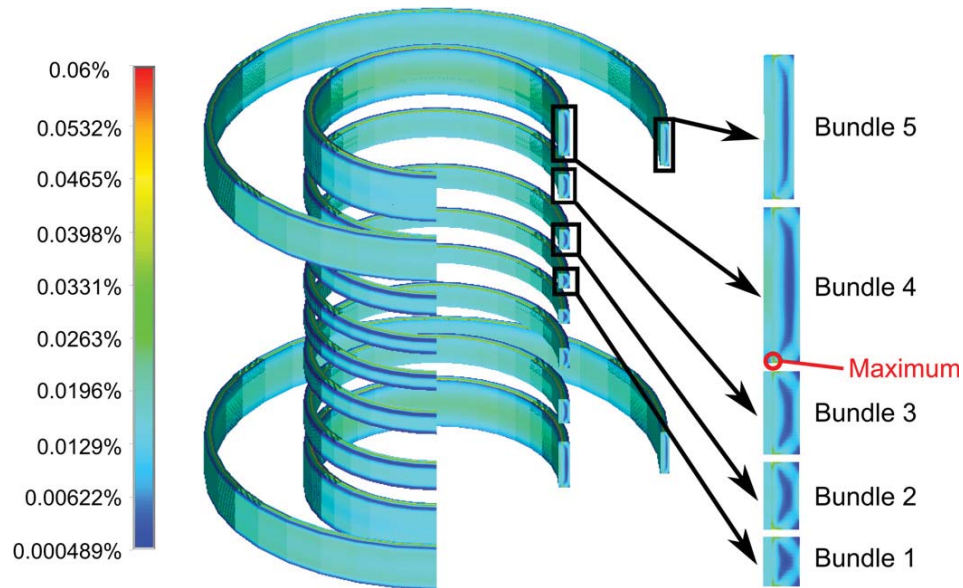

Figure 13. 1st principal mechanical strain in all five bundles of the coil at the time of electromagnetic charging after wire winding and cooling down to operating temperature.

−0.3% in the compressive direction at the time of electromagnetic operation [22, 23, 29, 62]. From the analysis of all five coil bundles, as principal strains are considered according to maximum strain criteria [60], the entire system develops a maximum mechanical strain of 0.016%, which is well below the design criterion of 0.2%. Also, the 3rd principal mechanical strain development is in the range of −0.035%, which is well below the −0.3% failure criterion. The entire coil bundle system is shown in figure 13 in a $\frac{3}{4}$th expansion of the axisymmetric bundle and total 1st principal mechanical strain is plotted. From the figure, the maximum mechanical strain of 0.06% is observed at the outermost axial location (direction 2 of wire) in coil bundle 4 which is also within the design criteria (−0.3% to 0.2%). Thus the analysis indicates the safe operation of the magnet for a design field of 1.5 T.

6. Conclusion

This article considers a conduction cooled MgB_2 superconducting magnet system designed specifically for a 1.5 T MRI machine. The system is modeled at three stages of manufacturing and operation: the winding of coil bundles in layers around a mandrel, the cool down of the magnets, and ultimately, the electromagnetic charging. The constituent wire and support matrix are considered as a composite of MgB_2 made up of niobium, monel, copper and epoxy. A combination of analytical approximations and FEA are used to verify the calculation of the stress and strain in the coil and mandrel, and the analysis is simplified by reducing the geometry to 2D axisymmetric at the mid-plane of the entire system.

After winding, cool-down and electromagnetic charging, the strain state of the coil bundles provides a clear image of the strain development of the entire system. It is determined that the failure criteria are the principal mechanical strains developed in the magnet bundle. The failure is initiated when an irreversible degradation occurs in the wire and the wire becomes resistive due to the strain exceeding −0.6% or 0.4% at the time of electromagnetic operation. For design purposes, considering a safety margin, a limit of −0.3% to 0.2% is imposed. From the FEA using ANSYS APDL, the maximum principal mechanical strain is estimated at ∼0.06% at the outermost axial location in coil bundle 4. All calculated strains are within the safety limit of −0.3% to 0.2% strain for MgB_2. Hence, it is expected that the entire magnet system is safe to operate with respect to strain development at 1.5 T. Finally, further studies will investigate the mechanical integrity of the magnet during a quench.

Acknowledgment

References

[1] Lvovsky Y and Jarvis P 2005 Superconducting systems for MRI-present solutions and new trends *IEEE Trans. Appl. Supercond.* **15** 1317–25

[2] Wang Z M 2013 Superconducting magnet of magnetic resonance imaging system *2013 IEEE Int. Conf. on Applied Superconductivity and Electromagnetic Devices (ASEMD)* pp 530–3

[3] Spencer C, Sanger P A and Young M 1979 The temperature and magnetic field dependence of superconducting critical current densities of multifilamentary Nb_3Sn and NbTi composite wires *IEEE Trans. Magn.* **15** 76–9

[4] Lvovsky Y, Stautner E W and Zhang T 2013 Novel technologies and configurations of superconducting magnets for MRI *Supercond. Sci. Technol.* **26** 093001

[5] Cai Z, Clarke R H, Glowacki B A, Nuttall W J and Ward N 2010 Ongoing ascent to the helium production plateau—insights from system dynamics *Resour. Policy* **35** 77–89

[6] Morita H, Okada M, Tanaka K, Sato J, Kitaguchi H, Kumakura H, Togano K, Itoh K and Wada H 2001 10 T conduction cooled Bi-2212/Ag HTS solenoid magnet system *IEEE Trans. Appl. Supercond.* **11** 2523–6

[7] Parkinson B J, Slade R, Mallett M J D and Chamritski V 2013 Development of a cryogen free 1.5 T YBCO HTS magnet for MRI *IEEE Trans. Appl. Supercond.* **23** 4400405

[8] Baig T, Yao Z, Doll D, Tomsic M and Martens M 2014 Conduction cooled magnet design for 1.5 T, 3.0 T and 7.0 T MRI systems *Supercond. Sci. Technol.* **27** 125012

[9] Miyazaki H, Iwai S, Tosaka T, Tasaki K, Hanai S, Urata M, Ioka S and Ishii Y 2013 Development of a 5.1 T conduction-cooled YBCO coil composed of a stack of 12 single pancakes *Physica* C **484** 287–91

[10] Young M A, Demko J A, Gouge M J, Pace M O, Lue J W and Grabovickic R 2003 Measurements of the performance of BSCCO HTS tape under magnetic fields with a cryocooled test rig *IEEE Trans. Appl. Supercond.* **13** 2964–7

[11] Wang Q, Song S, Lei Y, Dai Y, Zhang B, Wang C, Lee S and Kim K 2006 Design and fabrication of a conduction-cooled high temperature superconducting magnet for 10 kJ superconducting magnetic energy storage system *IEEE Trans. Appl. Supercond.* **16** 570–3

[12] Choi Y S, Kim D L, Lee B S, Yang H S and Painter T A 2009 Conduction-cooled superconducting magnet for material control application *IEEE Trans. Appl. Supercond.* **19** 2190–3

[13] Choi Y S, Kim D L, Yang H S, Lee B S and Jung W M 2009 Cryocooled cooling system for superconducting magnet *Proc. 15th Int. Cryocooler Conf.* pp 665–70

[14] Bud'ko S L, Lapertot G, Petrovic C, Cunningham C E, Anderson N and Canfield P C 2001 Boron isotope effect in superconducting MgB_2 *Phys. Rev. Lett.* **86** 1877–80

[15] Vinod K, Kumar R G A and Syamaprasad U 2007 Prospects for MgB_2 superconductors for magnet application *Supercond. Sci. Technol.* **20** R1

[16] Modica M, Angius S, Bertora L, Damiani D, Marabotto M, Nardelli D, Perrella M, Razeti M and Tassisto M 2007 Design, construction and tests of MgB_2 coils for the development of a cryogen free magnet *IEEE Trans. Appl. Supercond.* **17** 2196–9

[17] Yao W, Bascunan J, Kim W-S, Hahn S, Lee H and Iwasa Y 2008 A solid nitrogen cooled demonstration; coil for MRI applications *IEEE Trans. Appl. Supercond.* **18** 912–5

[18] Mine S, Xu M, Buresh S, Stautner W, Immer C, Laskaris E T, Amm K and Grasso G 2013 Second test coil for the development of a compact 3 T magnet *IEEE Trans. Appl. Supercond.* **23** 4601404

[19] Ling J, Voccio J, Kim Y, Hahn S, Bascunan J, Park D K and Iwasa Y 2013 Monofilament wire for a whole-body MRI magnet: superconducting joints and test coils *IEEE Trans. Appl. Supercond.* **23** 6200304

[20] Tomsic M, Rindfleisch M, Yue J, McFadden K, Phillips J, Sumption M D, Bhatia M, Bohnenstiehl S and Collings E W 2007 Overview of MgB$_2$ superconductor applications *Int. J. Appl. Ceram. Technol.* **4** 250–9

[21] Penco R and Grasso G 2007 Recent development of MgB$_2$-based large scale applications *IEEE Trans. Appl. Supercond.* **17** 2291–4

[22] Kováč P, Kopera L, Melišek T, Rindfleisch M, Haessler W and Hušek I 2013 Behaviour of filamentary MgB$_2$ wires subjected to tensile stress at 4.2 K *Supercond. Sci. Technol.* **26** 105028

[23] Dhallé M, Weeren H van, Wessel S, Ouden A den, Kate H H J ten, Hušek I, Kováč P, Schlachter S and Goldacker W 2005 Scaling the reversible strain response of MgB$_2$ conductors *Supercond. Sci. Technol.* **18** S253

[24] Li G Z, Yang Y, Susner M A, Sumption M D and Collings E W 2012 Critical current densities and *n*-values of MgB$_2$ strands over a wide range of temperatures and fields *Supercond. Sci. Technol.* **25** 025001

[25] Li G Z, Sumption M D, Susner M A, Yang Y, Reddy K M, Rindfleisch M A, Tomsic M J, Thong C J and Collings E W 2012 The critical current density of advanced internal-Mg-diffusion-processed MgB$_2$ wires *Supercond. Sci. Technol.* **25** 115023

[26] Yamamoto A, Shimoyama J, Ueda S, Katsura Y, Horii S and Kishio K 2005 Improved critical current properties observed in MgB$_2$ bulks synthesized by low-temperature solid-state reaction *Supercond. Sci. Technol.* **18** 116

[27] Ma Y, Zhang X, Nishijima G, Watanabe K and Bai X 2006 Significantly enhanced critical current densities in MgB$_2$ tapes made by a scaleable, nano-carbon addition route *Appl. Phys. Lett.* **88** 072502

[28] Dou S X, Soltanian S, Horvat J, Wang X L, Munroe P, Zhou S H, Ionescu M, Liu H K and Tomsic M 2002 Enhancement of the critical current density and flux pinning of MgB$_2$ superconductor by nanoparticle SiC doping *Appl. Phys. Lett.* **81** 3419

[29] Kitaguchi H and Kumakura H 2005 Superconducting and mechanical performance and the strain effects of a multifilamentary MgB$_2$/Ni tape *Supercond. Sci. Technol.* **18** S284

[30] Katagiri K, Takaya R, Kasaba K, Tachikawa K, Yamada Y, Shimura S, Koshizuka N and Watanabe K 2005 Stress–strain effects on powder-in-tube MgB$_2$ tapes and wires *Supercond. Sci. Technol.* **18** S351

[31] Guan M, Wang X, Ma L, Zhou Y and Xin C 2014 Magneto-mechanical coupling analysis of a superconducting solenoid magnet in self-magnetic field *IEEE Trans. Appl. Supercond.* **24** 1–4

[32] Schild T, Aubert G, Berriaud C, Bredy P, Juster F P, Meuris C, Nunio F, Quettier L, Rey J M and Vedrine P 2008 The iseult/inumac whole body 11.7 T MRI magnet design *IEEE Trans. Appl. Supercond.* **18** 904–7

[33] Li L, Cheng J, Ni Z, Wang H, Dai Y and Wang Q 2015 Preliminary mechanical analysis of a 9.4 T whole-body MRI magnet *IEEE Trans. Appl. Supercond.* **25** 1–7

[34] Jiang X, Guo Y, Chen J, Chai G, Liu S, Zhang T, Wang L, Yang T, Cheng H and Deng H 2013 A 7 T actively shielded superconducting magnet for animal MRI *IEEE Trans. Appl. Supercond.* **23** 4400604

[35] Wang Q *et al* 2012 A superconducting magnet system for whole-body metabolism imaging *IEEE Trans. Appl. Supercond.* **22** 4400905

[36] Dai Y *et al* 2012 Structural design of a 9.4 T whole-body MRI superconducting magnet *IEEE Trans. Appl. Supercond.* **22** 4900404

[37] Chen J and Jiang X 2012 Stress analysis of a 7 T actively shielded superconducting magnet for animal MRI *IEEE Trans. Appl. Supercond.* **22** 4903104

[38] Li L, Ni Z, Cheng J, Wang H, Wang Q and Zhao B 2012 Effect of pretension, support condition, and cool down on mechanical disturbance of superconducting coils *IEEE Trans. Appl. Supercond.* **22** 3800104

[39] Arp V 1977 Stresses in superconducting solenoids *J. Appl. Phys.* **48** 2026–36

[40] Caldwell J 1982 Electromagnetic forces in high field magnet coils *Appl. Math. Modelling* **6** 157–60

[41] Moon F C 1984 *Magneto-Solid Mechanics* (New York: Wiley)

[42] Wu W, He Y, Ma L Z, Huang W X, Yao Q G, Wu X, Guo B L, Zhang B, Yuan P and Xia J W 2010 Design of a 7 T superconducting magnet for lanzhou penning trap *IEEE Trans. Appl. Supercond.* **20** 989–92

[43] Wang Q *et al* 2012 A superconducting magnet system for whole-body metabolism imaging *IEEE Trans. Appl. Supercond.* **22** 4400905

[44] Guan M, Wang X, Xin C, Wu W and Ma L 2013 Structural mechanics exploration for multicomponent superconducting solenoids by Hoop strain tests during cooling and excitation *J. Supercond. Nov. Magn.* **27** 1179–85

[45] Barbero E J 2013 *Finite Element Analysis of Composite Materials Using ANSYS*® 2nd edn (Boca Raton, FL: CRC Press)

[46] Luciano R and Sacco E 1998 Variational methods for the homogenization of periodic heterogeneous media *Eur. J. Mech.* A **17** 599–617

[47] Collins B 2013 Investigation of Nb$_3$Sn based superconductors through hierarchical models *PhD Dissertation* UC Berkeley

[48] Boso D P 2013 A simple and effective approach for thermo-mechanical modelling of composite superconducting wires *Supercond. Sci. Technol.* **26** 045006

[49] Boso D P, Lefik M and Schrefler B A 2006 Homogenisation methods for the thermo-mechanical analysis of Nb$_3$Sn strand *Cryogenics* **46** 569–80

[50] Prikhna T A 2009 Properties of MgB$_2$ bulk arXiv:0912.4906

[51] Neumeier J J, Tomita T, Debessai M, Schilling J S, Barnes P W, Hinks D G and Jorgensen J D 2005 Negative thermal expansion of MgB$_2$ in the superconducting state and anomalous behavior of the bulk Grüneisen function *Phys. Rev.* B **72** 220505

[52] http://copper.org/resources/properties/cryogenic/

[53] https://en.wikipedia.org/wiki/Niobium

[54] White G K 1962 Thermal expansion of vanadium, niobium, and tantalum at low temperatures *Cryogenics* **2** 292–6

[55] http://specialmetals.com/assets/documents/alloys/monel/monel-alloy-400.pdf

[56] http://ncsx.pppl.gov/NCSX_Engineering/Materials/InsulationProperties/CTD-101K_Datasheet_2003.pdf

[57] Jensen J E, Stewart R G, Tuttle W A and Brechna H 1980 *Brookhaven National Laboratory Selected Cryogenic Data Notebook: Sections X-XVIII* vol 2 (New York: Brookhaven National Laboratory)

[58] Bobrov E S, Williams J E C and Iwasa Y 1985 Experimental and theoretical investigation of mechanical disturbances in epoxy-impregnated superconducting coils: II. Shear-stress-induced epoxy fracture as the principal source of premature quenches and training theoretical analysis *Cryogenics* **25** 307–16

[59] Pasztor G and Schmidt C 1978 Dynamic stress effects in technical superconductors and the 'training' problem of superconducting magnets *J. Appl. Phys.* **49** 886–99

[60] Orifici A C, Herszberg I and Thomson R S 2008 Review of methodologies for composite material modelling incorporating failure *Compos. Struct.* **86** 194–210

[61] Vaghar M R, Garmestani H and Markiewicz W D 1996 Elastoplastic stress analysis of Nb_3Sn superconducting magnet *J. Appl. Phys.* **80** 2490

[62] Zhou C, Gao P, Krooshoop H J G, Dhallé M, Sumption M D, Rindfleisch M, Tomsic M, Kulich M, Senatore C and Nijhuis A 2014 Intrawire resistance, AC loss and strain dependence of critical current in MgB_2 wires with and without cold high-pressure densification *Supercond. Sci. Technol.* **27** 075002

[63] De Groot R, Peters M C, De Haan Y M, Dop G J and Plasschaert A J 1987 Failure stress criteria for composite resin *J. Dent. Res.* **66** 1748–52

[64] Kovác P, Dhallé M, Melišek T, Eck H J N, van, Wessel W A J, ten Haken B and Hušek I 2003 Dependence of the critical current in *ex situ* multi- and mono-filamentary MgB_2/Fe wires on axial tension and compression *Supercond. Sci. Technol.* **16** 600